Journal of Geophysical Research: Space Physics

RESEARCH ARTICLE
10.1029/2018JA025543

Special Section:
Mars Aeronomy

This article is a companion to Dong et al. (2015) https://doi.org/10.1002/2015JA020990.

Key Points:
- Despite the similar ion loss rate calculated from 1-D and 3-D atmospheres, the latter are required to adequately reproduce MAVEN observations
- The hot oxygen corona plays an important role in protecting the Martian ionosphere/thermosphere from the solar wind erosion
- The thermospheric oxygen atom is the primary neutral source for O^+ ion escape during the relatively weak solar cycle 24

Correspondence to:
C. Dong,
dcfy@princeton.edu

Citation:
Dong, C., Bougher, S. W., Ma, Y., Lee, Y., Toth, G., Nagy, A. F., et al. (2018). Solar wind interaction with the Martian upper atmosphere: Roles of the cold thermosphere and hot oxygen corona. *Journal Geophysical Research: Space Physics*, *123*, 6639–6654. https://doi.org/10.1029/2018JA025543

Received 2 APR 2018
Accepted 22 JUN 2018
Accepted article online 28 JUN 2018
Published online 29 AUG 2018

Solar Wind Interaction With the Martian Upper Atmosphere: Roles of the Cold Thermosphere and Hot Oxygen Corona

Chuanfei Dong[1,2], Stephen W. Bougher[3], Yingjuan Ma[4], Yuni Lee[5], Gabor Toth[3], Andrew F. Nagy[3], Xiaohua Fang[6], Janet Luhmann[7], Michael W. Liemohn[3], Jasper S. Halekas[8], Valeriy Tenishev[3], David J. Pawlowski[9], and Michael R. Combi[3]

[1]Department of Astrophysical Sciences, Princeton University, Princeton, NJ, USA, [2]Princeton Center for Heliophysics, Princeton Plasma Physics Laboratory, Princeton University, Princeton, NJ, USA, [3]Department of Climate and Space Sciences and Engineering, University of Michigan, Ann Arbor, MI, USA, [4]Department of Earth and Space Sciences, Los Angeles, CA, USA, [5]NASA Goddard Space Flight Center, Greenbelt, MD, USA, [6]Laboratory for Atmospheric and Space Physics, University of Colorado Boulder, Boulder, CO, USA, [7]Space Sciences Laboratory, University of California, Berkeley, CA, USA, [8]Department of Physics and Astronomy, University of Iowa, Iowa City, IA, USA, [9]Department of Physics and Astronomy, Eastern Michigan University, Ypsilanti, MI, USA

Abstract We study roles of the thermosphere and exosphere on the Martian ionospheric structure and ion escape rates in the process of the solar wind-Mars interaction. We employ a four-species multifluid magnetohydrodynamic model to simulate the Martian ionosphere and magnetosphere. The *cold* thermosphere background is taken from the Mars Global Ionosphere Thermosphere Model, and the hot oxygen exosphere is adopted from the Mars exosphere Monte Carlo model—Adaptive Mesh Particle Simulator. A total of four cases with the combination of 1-D (globally averaged) and 3-D thermospheres and exospheres are studied. The ion escape rates calculated by adopting 1-D and 3-D atmospheres are similar; however, the latter are required to adequately reproduce the ionospheric observations by the Mars Atmosphere and Volatile EvolutioN mission. In addition, our simulations show that the 3-D hot oxygen corona plays an important role in preventing planetary molecular ions (O_2^+ and CO_2^+) escaping from Mars, mainly resulting from the mass loading of the high-altitude exospheric O^+ ions. The *cold* thermospheric oxygen atom, however, is demonstrated to be the primary neutral source for O^+ ion escape during the relatively weak solar cycle 24.

1. Introduction

Unlike Earth and Venus, Mars with a relatively weak surface gravity allows an extended corona of hot oxygen that can partially escape to space (Fox, 1993; Ip, 1988; Nagy & Cravens, 1988; Wallis, 1978). Being the most important reaction, the dissociative recombination of O_2^+ (deep in the dayside thermosphere/ionosphere) is responsible for producing most of dayside exospheric hot atomic oxygen ($O_2^+ + e \longrightarrow O^* + O^*$); therefore, the distribution of the hot oxygen exosphere is asymmetric around the Mars globe (Lee, Combi, Tenishev, Bougher, Lillis, 2015; Valeille et al., 2009). Note that it is not only the model that shows the hot O distribution is asymmetric, but it is also seen in the Mars Atmosphere and Volatile EvolutioN (MAVEN) Imaging Ultraviolet Spectrograph data (e.g., Leblanc et al., 2017; Lee, Combi, Tenishev, Bougher, Deighan, et al., 2015). In addition to the dissociative recombination of O_2^+, the sputtering caused by collisions between the pickup ions (e.g., O^+) and the Martian thermospheric background may also be an important source for the hot corona (Johnson & Luhmann, 1998; Leblanc et al., 2018; Luhmann & Kozyra, 1991). Compared with the *cold* thermospheric background, the *hot* (or energetic) oxygen has a thermal speed, $\langle v_O \rangle = (2k_B T_O/m_O)^{\frac{1}{2}}$, higher than the local thermal speed of the thermosphere.

Besides the strong day-night asymmetry exhibited in the hot oxygen density distribution, the major neutral species in the Martian thermosphere (CO_2 and O) are also distributed asymmetrically about the planet (e.g., Bougher et al., 2008; Bougher, Pawlowski, et al., 2015). Specifically, more neutral CO_2 molecules are in the dayside thermosphere than on the nightside at a given altitude because the CO_2 global distribution is mainly controlled by the global temperature instead of the dynamics. Therefore, the thermospheric CO_2 density increases (decreases) on the dayside (nightside) where temperatures are higher (lower). The density

distribution of atomic O (especially on the nightside), however, is mainly controlled by the day-night transport due to its relatively low mass; photochemistry may make certain contribution on the dayside oxygen density distribution. For atomic O, transport begins to have an effect as the thermospheric winds increase with increasing altitude above the region where dayside O is produced photochemically; the day-to-night atomic O distribution is impacted strongly by winds roughly above ~130 km (Bougher, Pawlowski, et al., 2015). The neutral wind can transport atomic O from dayside to nightside, resulting in a bulge of neutral O in the nightside thermosphere (Bougher, Pawlowski, et al., 2015).

In order to capture the asymmetry in the Martian thermosphere and exosphere, three-dimensional "whole atmosphere" (from the ground to the exobase, 0 to ~250 km; Bougher, Pawlowski, et al., 2015) and exosphere (Lee, Combi, Tenishev, Bougher, Lillis, 2015) models are ultimately required to capture these asymmetric features. The modeled thermosphere and exosphere can be further input into a global plasma code as the neutral background, such that roles of the 3-D thermosphere and exosphere on the Martian ionospheric structure and ion escape processes can be investigated in detail. Note that the incident solar wind at Mars encounters an extended hot exosphere, a conductive ionosphere, and highly localized crustal magnetic fields (the strongest of which in the southern hemisphere [Acuña et al., 1999]), resulting in a complex obstacle to the solar wind that varies on all spatial and temporal scales. Among all the objects in the solar system, Mars, therefore, offers a uniquely challenging set of conditions to simulate.

In recent years, investigations of the Martian thermosphere/ionosphere structure (e.g., Bougher, Jakorsky, et al., 2015; Withers et al., 2015), magnetic topology (e.g., DiBraccio et al., 2018; Liemohn et al., 2017; Luhmann et al., 2015; Xu et al., 2016), and atmospheric ion escape rates (e.g., Egan et al., 2018; Fang et al., 2017; Halekas et al., 2016) have become increasingly important because they are closely related to the evolution of the Martian atmosphere and can affect its climate over the past four billion years (e.g., Bougher, Cravens, et al., 2015; Dong, Lee, et al., 2018; Jakosky, Lin, et al., 2015; Lillis et al., 2015; Mansfield et al., 2018, and the references therein). In situ spacecraft measurements (e.g., Brain et al., 2015; Dong, Fang, et al., 2015; Lundin et al., 2013; Ramstad et al., 2015) have greatly improved our estimates of global ion loss rates at the current epoch. By using Mars Express Analyzer of Space Plasmas and Energetic Atoms 3 data from June 2007 to January 2013, Lundin et al. (2013) reported that the average heavy ion escape rate increased approximately by a factor of 10, from 1×10^{24} s^{-1} (solar minimum) to 1×10^{25} s^{-1} (solar maximum). More recently, Brain et al. (2015) analyzed 4 months of Mars Atmosphere and Volatile EvolutioN (MAVEN) spacecraft data and estimated a net ion escape rate of $\sim 2.5 \times 10^{24}$ s^{-1} by choosing a spherical shell at ~1,000 km above the planet with energies >25 eV during solar cycle maximum conditions. In addition, Liemohn et al. (2014) and Dong, Fang, et al. (2015) confirmed the substantial plume-like distribution of escaping ions from the Martian atmosphere in Mars Express and MAVEN observations, organized by the upstream solar wind convection electric field. It is also worth noting that the total ion loss rate increased by more than 1 order of magnitude during an interplanetary corona mass ejection event observed by MAVEN on 8 March 2015 (Curry, Luhmann, Ma, Dong, et al., 2015; Dong, Ma, et al., 2015; Jakosky, Grebowsky, et al., 2015; Luhmann et al., 2017; Ma et al., 2017). Moreover, Lingam et al. (2018) found that the solar energetic protons associated with extreme space weather events with energies $\gtrsim$150 MeV can reach the Martian surface; the same cutoff value has also been presented by the Mars Science Laboratory's Curiosity rover group (Hassler et al., 2014).

In order to study the solar wind interaction with the Martian upper atmosphere, various plasma fluid models and kinetic particle codes have been developed. A few notable examples include the multispecies single-fluid magnetohydrodynamic (MHD) models (Ma et al., 2004, 2014), the multifluid MHD (MF-MHD) models (Dong, Bougher, Ma, Toth, Nagy, et al., 2014, Dong, Bougher, et al., 2015; Harnett & Winglee, 2006; Najib et al., 2011; Riousset et al., 2013, 2014), the test particle approach (Curry et al., 2014, Curry, Luhmann, Ma, Liemohn, et al., 2015; Fang et al., 2008, 2010a) and the hybrid particle-in-cell (hybrid-PIC) codes (Brecht et al., 2016; Modolo et al., 2016). These codes have been used to help quantify the ion escape rates from the Martian upper atmosphere through the solar wind-Mars interaction. Most of these studies can reach a reasonable agreement with the spacecraft observations. However, until now no systematic study was focused on the influence of 3-D thermospheres and exospheres on the Martian ionospheric structure and ion escape rates.

In this paper, we adopt the 3-D Mars thermosphere (i.e., neutral temperatures T_n, neutral densities n_O and n_{CO_2}, and photoionization frequencies I_O and I_{CO_2}) from the Mars Global Ionosphere Thermosphere Model (M-GITM; Bougher, Pawlowski, et al., 2015) and the hot atomic oxygen density, $n_{O_{hot}}$, from the Mars exosphere Monte Carlo model — Adaptive Mesh Particle Simulator (AMPS; Lee, Combi, Tenishev, Bougher, Lillis, 2015). M-GITM

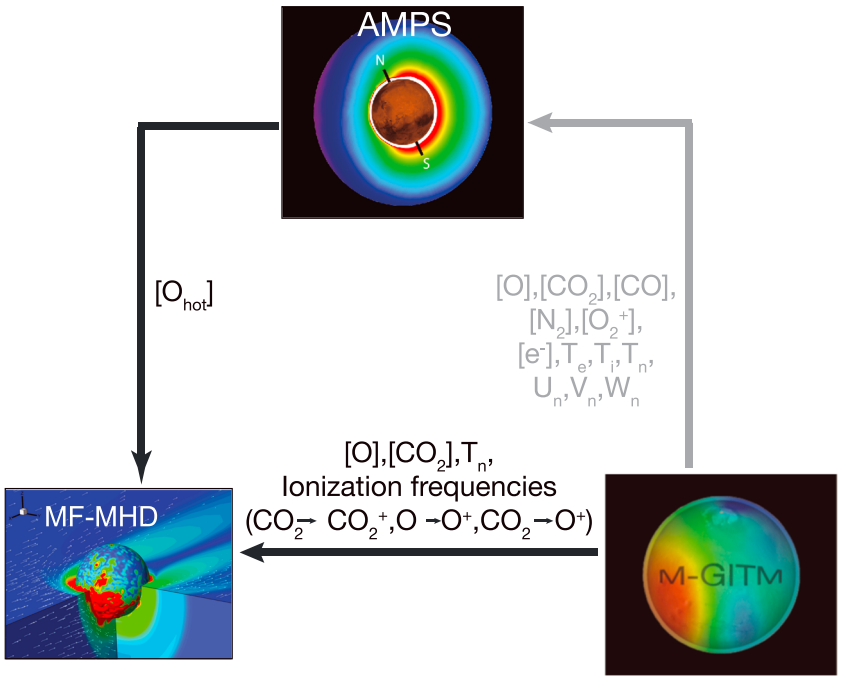

Figure 1. Sketch of a one-way coupling approach between M-GITM, Mars AMPS, and the MF-MHD model (after Figure 1 of Dong, Bougher, et al., 2015). The notation T_n denotes the neutral atmospheric temperature. The quantities [O], [CO_2], and [O_{hot}] are the thermospheric *cold* O, CO_2, and exospheric *hot* O number densities, respectively. In this study, we adopt the one-way coupling indicated by the solid black lines. For the detailed study of the one-way coupling between M-GITM and Mars AMPS (solid gray line), please refer to Lee, Combi, Tenishev, Bougher, Lillis (2015). AMPS = Adaptive Mesh Particle Simulator; M-GITM = Mars Global Ionosphere Thermosphere Model; the MF-MHD model = the multifluid magnetohydrodynamic model.

and Mars AMPS are one-way coupled with the 3-D Block-Adaptive-Tree-Solarwind-Roe-Upwind-Scheme (BATS-R-US) Mars MF-MHD model (Dong, Bougher, Ma, Toth, Nagy, et al., 2014; Dong, Bougher, et al., 2015; Najib et al., 2011; see Figure 1 for the one-way coupled framework). The Mars AMPS hot oxygen corona is calculated based on the thermosphere/ionosphere background from M-GITM (Lee, Combi, Tenishev, Bougher, Lillis, 2015). In the present work, the simulations are carried out for four selected cases with the combination of 1-D and 3-D neutral atmospheres.

The remainder of this paper is divided into three sections. In section 2, we briefly introduce the three models employed in this study. In section 3.1, we investigate the role of the 3-D thermosphere on the Martian ionospheric structure and ion escape rates by means of data-model and model-model comparisons. In section 3.2, we study the effect of the 3-D exosphere on the ion escape rate and the corresponding molecular to atomic escaping ion ratio $(O_2^+ + CO_2^+)/O^+$ through model-model comparisons. Conclusions are summarized in section 4.

2. Model Description

In this section, M-GITM, AMPS, and the MF-MHD model are briefly introduced. All these models have been adopted to support the MAVEN mission activities (2014–2018).

2.1. Mars Global Ionosphere Thermosphere Model

M-GITM (Bougher, Pawlowski, et al., 2015) combines the terrestrial GITM framework (Deng et al., 2008; Ridley et al., 2006) with the fundamental physical parameters, ion-neutral chemistry, and key radiative processes for Mars in order to capture the basic observed features of the thermal, compositional, and dynamical structure of the Mars atmosphere from the ground to the exobase (0–250 km). M-GITM currently solves for three-dimensional neutral and ion densities, as well as neutral temperatures and winds around the globe. Key neutral species presently include CO_2, CO, O, N_2, O_2, Ar, and He. Five key photochemical ion species currently include O^+, O_2^+, CO_2^+, N_2^+, and NO^+. Typically, production runs are conducted for a 5 × 5° longitude-latitude grid, with a constant 2.5-km vertical resolution (~0.25 scale height, $H_s = k_B T/mg$, where k_B is Boltzmann

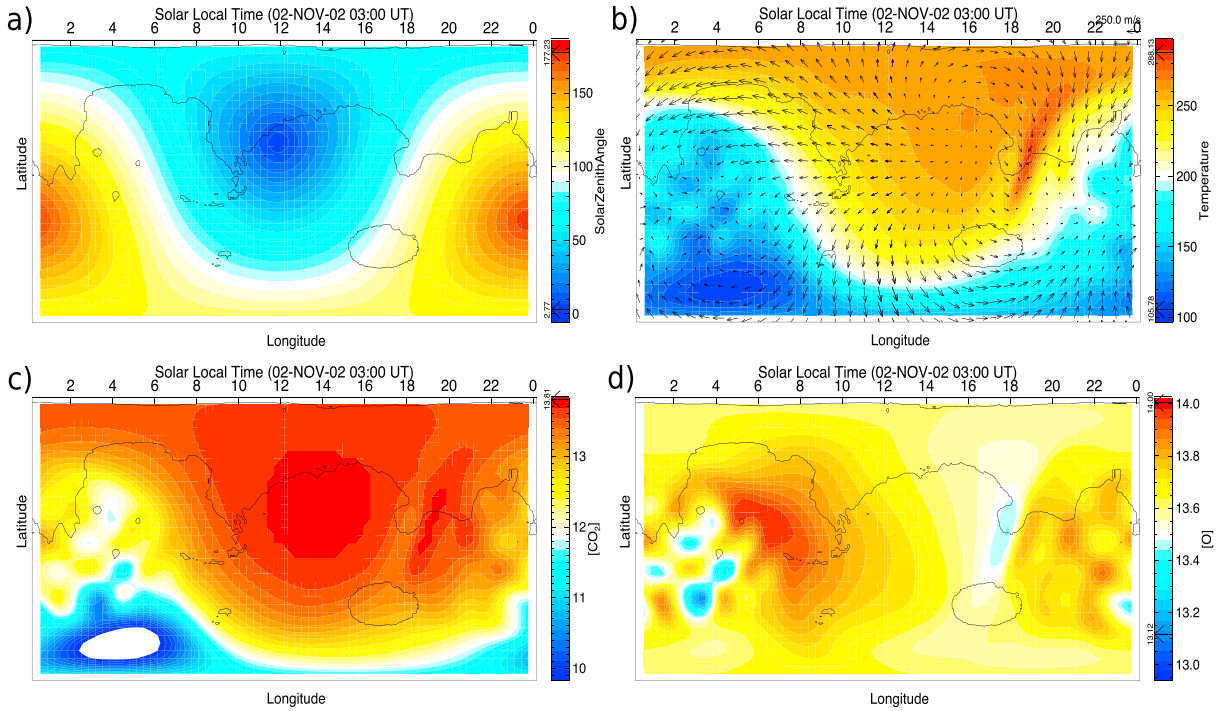

Figure 2. The color contours of (a) solar zenith angle (in degrees), (b) temperature (in kelvins), (c) log10 CO_2 densities (in m^{-3}), and (d) log10 atomic O densities (in m^{-3}) at ~200-km (exobase) altitude for aphelion solar moderate conditions ($Ls = 90$, $F_{10.7} = 130$). The arrows in Figure 2b indicate the relative magnitude and the direction of the horizontal winds. All the vertical axes (i.e., latitude) range from −90° to 90° . The white color highlights the regions below the low saturation of the color bar. UT = universal time.

constant, g is the acceleration due to planetary gravity, T is the neutral temperature, and m is the mass of the neutral species).

M-GITM validation studies thus far have focused upon simulations for a range of solar cycles and seasonal conditions (Bougher, Pawlowski, et al., 2015; Bougher, Jakorsky, et al., 2015, 2017). Figure 2a shows the solar zenith angle (SZA) distribution around Mars' globe for aphelion solar moderate conditions (APHMOD) in the geographic coordinate system. The subsolar point (i.e., where SZA = 0) is located in the northern hemisphere. An inspection of Figure 2b reveals that solar-driven exobase temperatures peak in the middle afternoon at the subsolar latitude (25° N). The warmer temperature near the evening terminator (LT = 18) is a result of the dynamical heating due to the convergent zonal winds (Bougher, Pawlowski, et al., 2015). The asymmetric distribution of CO_2 in latitude (Figure 2c) is closely related to the asymmetric diurnal temperature distribution (Figure 2b). Conversely, Figure 2d presents atomic oxygen density distributions for which dayside-produced O is transported to the nightside by the thermospheric wind system, where it subsequently accumulates at low-to-middle latitudes around LT = 4–8. All the features shown in Figure 2 indicate the importance of adopting the 3-D M-GITM thermosphere in a global plasma model in order to reproduce the ionospheric structure and accurately estimate the ion escape rates in the process of the solar wind-Mars interaction.

2.2. Mars AMPS

The code we employ to model the Martian exosphere is the 3-D Mars AMPS, which runs in the test particle mode using the Direct Simulation Monte Carlo (DSMC) method (Bird, 1994). The AMPS code (Lee, Combi, Tenishev, Bougher, Lillis, 2015; Tenishev & Combi, 2008; Tenishev et al., 2013a) is a well-tested code for a wide range of kinetic problems in rarefied gas regime. Examples of the AMPS applications include the cometary coma and the exospheres of Mars, Mercury, and the Moon. The 3-D structure and photochemical loss of hot oxygen particles from Mars have been investigated by taking advantage of the one-way coupled framework between Mars AMPS and M-GITM (Lee, Combi, Tenishev, Bougher, Deighan, et al., 2015; Lee, Combi, Tenishev, Bougher, Lillis, 2015). As shown in Figure 1, AMPS calculates the hot atomic oxygen density distribution based on the thermospheric background (i.e., neutral species O, CO_2, N_2, and CO) from M-GITM.

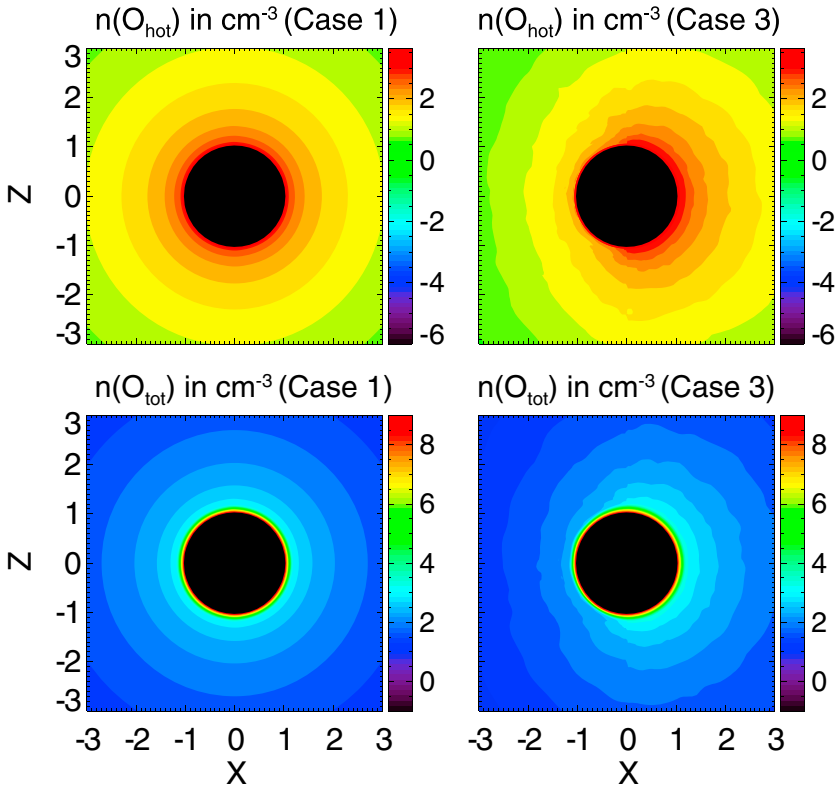

Figure 3. Comparisons of the hot atomic oxygen (first row) and total atomic oxygen (the sum of thermal and hot components, second row) density distribution (in cm^{-3}) from the globally averaged 1-D spherically symmetric Adaptive Mesh Particle Simulator profile (left) and the 3-D profile (right) in the $X - Z$ meridian plane in the Mars-centered Solar Orbital coordinate system. Both cases are based on the aphelion solar moderate conditions.
Note the use of different logarithmic scales.

Compared with the previous version where it assumed idealized hard sphere collisions and only isotropic scattering in the center of mass frame (Valeille et al., 2009), the current AMPS considers a more realistic description for the collisions between hot O and ambient species by adopting a forward scattering collision scheme with the angular differential scattering cross sections from Kharchenko et al. (2000). The related integrated cross sections (in square centimeters) are 1.2×10^{-14} for O-CO_2, 6.4×10^{-15} for O-O, and 1.8×10^{-14} for both O-N_2 and O-CO. The current AMPS (by adopting the forward scattering scheme) produces a more intensive (and closer to observed) hot oxygen corona than the previous case by adopting the isotropic scattering scheme and thus enhances the corresponding photochemical escape rate (Lee, Combi, Tenishev, Bougher, Lillis, 2015). However, there still exists certain discrepancy between MAVEN observations and AMPS predictions (Lee, Combi, Tenishev, Bougher, Lillis, 2015); further improvement of model predications of hot oxygen corona is an ongoing MAVEN effort.

The motion of each hot particle is influenced by the gravitational field of the Mars and modified by collisions with the background thermospheric species. The collision in the code depends on the rate of change in the background densities (i.e., rate of change in collision frequency). Although the nominal cell size is about 60 km at the model lower boundary (at 100-km altitude above the Martian surface), the large grid size does not prevent AMPS from capturing the variation in the Martian ionosphere and thermosphere. In AMPS, each macroparticle is initialized based on the thermospheric background prescribed by M-GITM (stored in an additional data table) at its resolution. It is noteworthy that the hybrid-PIC codes (e.g., Brecht et al., 2016; Modolo et al., 2016) have similar grid resolution for studying the solar wind-Mars interaction. The AMPS computational domain extends to six Mars radius (one Mars radius, $R_M \approx 3{,}396$ km).

Figure 3 illustrates the hot and total (the sum of thermal and hot components) atomic oxygen distribution around the Mars globe in a logarithmic scale. Figure 3 is based on the Mars-centered Solar Orbital (MSO)

Table 1
Chemical Reactions and Associated Rates in Mars Multifluid Magnetohydrodynamic Code

Chemical reaction	Rate
Primary photolysis and particle impact	(s^{-1})
$CO_2 + h\nu \rightarrow CO_2^+ + e^-$	8.37×10^{-7}
$CO_2 + h\nu \rightarrow CO + O^+ + e^-$	7.52×10^{-8}
$O + h\nu \rightarrow O^+ + e^-$	1.52×10^{-7}
$H + h\nu \rightarrow H^+ + e^-$	5.58×10^{-8}
$e^- + H \rightarrow e^- + H^+ + e^-$	See text
$e^- + O \rightarrow e^- + O^+ + e^-$	See text
Ion-neutral chemistry	($cm^3\ s^{-1}$)
$CO_2^+ + O \rightarrow O_2^+ + CO$	1.64×10^{-10}
$CO_2^+ + O \rightarrow O^+ + CO_2$	9.60×10^{-11}
$O^+ + CO_2 \rightarrow O_2^+ + CO$	$1.1 \times 10^{-9}\ (800/T_i)^{0.39}$
$O^+ + H \rightarrow H^+ + O$	6.4×10^{-10}
$H^+ + O \rightarrow O^+ + H$	5.08×10^{-10}
Ion-electron recombination chemistry	($cm^3\ s^{-1}$)
$O_2^+ + e^- \rightarrow O + O$	$7.38 \times 10^{-8}\ (1200/T_e)^{0.56}$
$CO_2^+ + e^- \rightarrow CO + O$	$3.10 \times 10^{-7}\ (300/T_e)^{0.5}$

Note. The ion-neutral and ion-electron chemical reaction rates are adopted from Najib et al. (2011), while the photoionization frequencies (at the top of atmosphere for aphelion solar moderate conditions) are adopted from Bougher, Pawlowski, et al. (2015) as indicated in Figure 1.

coordinate system, where the $+X$ axis points from Mars to the Sun, the $+Z$ axis is perpendicular to the Martian orbital plane and points northward, and the Y axis completes the right-hand system. The left panels correspond to the global hot and total O distributions of the 1-D spherically symmetric case, that is, by averaging overall the longitudes and latitudes from the 3-D AMPS output, $\bar{n}(r) = \frac{\iint n(r,\theta,\phi)\sin\theta d\theta d\phi}{\iint \sin\theta d\theta d\phi}$. The right panels show the original 3-D AMPS and M-GITM output. An inspection of the second row of Figure 3 reveals that the thermal atomic oxygen dominates over the hot component at relatively low altitudes (i.e., in the thermosphere), while the hot atomic oxygen is the dominant neutral species at relatively high altitudes (i.e., in the exosphere). Both panels are for the APHMOD. The 3-D AMPS hot oxygen corona shows a great day-night asymmetry, which cannot be captured by a 1-D spherically symmetric profile. The remarkable asymmetry shown in Figure 3 indicates the significance of adopting the 3-D hot oxygen corona in a global plasma code for studying the Martian atmospheric ion loss.

2.3. BATS-R-US Mars MF-MHD Model

The 3-D BATS-R-US MF-MHD model solves separate continuity, momentum, and energy equations for each fluid (Dong et al., 2017; Glocer et al., 2009; Huang et al., 2016; Najib et al., 2011; Powell et al., 1999; Tóth et al., 2012). For the Mars version, it solves MHD equations for four ion fluids H^+, O^+, O_2^+, and CO_2^+ (Dong, Bougher, Ma, Toth, Nagy, et al., 2014; Dong, Bougher, et al., 2015; Najib et al., 2011). Interestingly, Rubin et al. (2014) showed that by using an MF-MHD model, it can mimic some major features obtained with the hybrid-PIC

Table 2
Input Parameters Used for Different Cases

Simulation #	Subsolar position of periapsis	Neutral atmosphere	Solar cycle conditions
Case 1	167.9° E, 24.9° N	1-D_{cold} and 1-D_{hot}	Aphelion solar
Case 2	167.9° E, 24.9° N	3-D_{cold} and 1-D_{hot}	moderate conditions
Case 3	167.9° E, 24.9° N	3-D_{cold} and 3-D_{hot}	
Case 4	167.9° E, 24.9° N	3-D_{cold} without O_{hot}	

Note. The solar cycle conditions are chosen based upon one Mars Atmosphere and Volatile EvolutioN trajectory (orbit O2349) on 14 December 2015, during which it has a dayside periapsis.

Table 3
Solar Wind Input Parameters Used for Different Cases

Simulation #	n_{sw} (cm^{-3})	v_{sw} (km/s)	IMF (nT)	T_{sw}^{proton} and $T_{sw}^{electron}$ (K)
Cases 1–4	4.85	(−348.5, −7.0, −25.5)	(−0.25, 5.5, −1.0)	5.9×10^4 and 1.3×10^5

Note. The solar wind inputs are taken from Mars Atmosphere and Volatile EvolutioN measurements on 14 December 2015 (orbit O2349), during which it has a steady solar wind and interplanetary magnetic field (IMF).

calculation for a weak comet, such as the finite gyration effect of the planetary/cometary heavy ions and the associated pickup processes. The underlying reason is that MF-MHD includes the dynamics of individual ion species. The Lorentz force term, $\propto (\mathbf{u_s} - \mathbf{u_+}) \times \mathbf{B}$, in the individual ion momentum equation is mainly responsible for the asymmetric ion escape plume and the associated pickup processes, resulting from the difference between the charge averaged ion velocity, $\mathbf{u}_+$, and the individual fluid velocity, $\mathbf{u_s}$, of species s (Dong, Bougher, Ma, Toth, Nagy, et al., 2014).

At the MF-MHD model lower boundary (100 km above the Martian surface), the densities of O^+, O_2^+, and CO_2^+ satisfy the photochemical equilibrium condition (e.g., Schunk & Nagy, 2009, chapters 8 and 13). A reflective inner boundary condition for the velocity **u** is used, which leads to an approximately zero velocity at the inner boundary as expected. The plasma temperature is set to be twice the value of the neutral temperature at the inner boundary, where both ions and electrons have roughly the same temperature as neutrals due to collisions. We use the 60° harmonic expansion model of Arkani-Hamed (2001) to describe the crustal magnetic fields at Mars (Acuña et al., 1999). The photochemical reactions in the model include charge exchange, photoionization, electron impact ionization and ion-electron recombination. The electron impact ionization rates are given by Cravens et al. (1987). The elastic collision frequencies are taken from Schunk and Nagy (2009). Table 1 summarizes the chemical reactions and the associated rates for inelastic collisions used in the MF-MHD calculations.

The smallest radial resolution is about 5 km at the inner boundary, while the grid size can increase to several thousand kilometers at the outer boundary (~30 R_M) due to the nonuniformity in the mesh design. The angular resolution varies from 1.5° to 3.0° in a spherical grid mesh bounded by a cube with $-30R_M \le X \le 8R_M$; $-30R_M \le Y, Z \le 30R_M$.

3. Simulation Results and Discussion

In this section, we discuss the simulation results obtained by using the one-way coupling approach, that is, both the M-GITM and AMPS neutral profiles are used as the input for the MF-MHD model (Figure 1). Firstly, in order to study the effect of the 3-D thermosphere on the Martian ionospheric structure and ion escape rates, we adopt either the 1-D globally averaged (and thus spherically symmetric) thermosphere (Case 1) or the 3-D M-GITM thermosphere (Case 2) while fixing the 1-D globally averaged hot oxygen corona. Detailed data-model comparison along a selected MAVEN trajectory on 14 December 2015 (orbit O2349) is studied. As an illustrative example, we also present the global ionospheric ion distribution at a constant altitude, 200 km, for both Cases 1 and 2. In section 3.2, we investigate the role of the 3-D exosphere on the ion escape rate. Three cases are studied for the APHMOD with a 1-D corona, a 3-D corona, and a case without a hot oxygen corona (Cases 2–4). Tables 2 and 3 summarize the parameters used for each case. The ion escape rates are summarized in Table 4.

Table 4
Calculated Ion Escape Rates (in $\times10^{24}$ s^{-1}) and Molecular to Atomic Escaping Ion Ratio Listed in the Last Column

Simulation cases	O^+	O_2^+	CO_2^+	Total	$(O_2^+ + CO_2^+)/O^+$
Case 1 (1-D_{cold} and 1-D_{hot})	0.57	1.45	0.29	2.30	3.06
Case 2 (3-D_{cold} and 1-D_{hot})	0.74	1.27	0.27	2.28	2.09
Case 3 (3-D_{cold} and 3-D_{hot})	0.89	1.18	0.31	2.38	1.67
Case 4 (3-D_{cold} and noO_{hot})	0.88	1.52	0.40	2.80	2.17

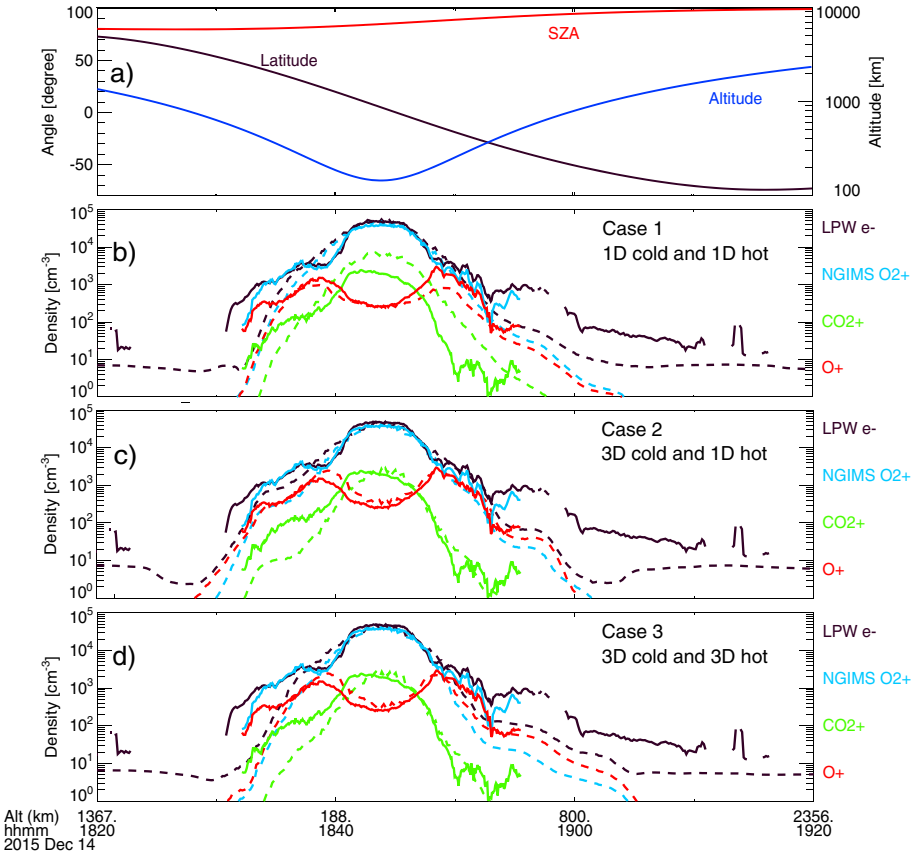

Figure 4. Comparisons of the ion and electron densities between the multifluid magnetohydrodynamic simulations (dashed lines) and the Mars Atmosphere and Volatile EvolutioN observations (solid lines). The ion and electron densities are measured by NGIMS and LPW, respectively. Second panel: Case 1 with 1-D thermosphere and 1-D exosphere. Third panel: Case 2 with 3-D thermosphere and 1-D exosphere. Fourth panel: Case 3 with 3-D thermosphere and 3-D exosphere. LPW = Langmuir Probe and Waves; NGIMS = Neutral Gas and Ion Mass Spectrometer.

3.1. Effects of 3-D Thermosphere on the Solar Wind-Mars Interaction

We first focus on the effect of the 3-D thermosphere on the solar wind-Mars interaction. Figure 4 presents the data-model comparison of the ionospheric density profiles between the MF-MHD calculations (dashed lines) and the MAVEN data (solid lines). The electron density was measured by the Langmuir Probe and Waves instrument on board the spacecraft. The O^+, O_2^+, and CO_2^+ ion densities were measured by the Neutral Gas and Ion Mass Spectrometer. Figure 4a depicts the spacecraft altitudes (blue), latitude (black) and SZA (red) versus time along the trajectory. The rest of the panels are the detailed data-model comparisons based on the 1-D thermosphere and exosphere (Case 1, Figure 4b), the 3-D thermosphere and the 1-D exosphere (Case 2, Figure 4c), and the 3-D thermosphere and exosphere (Case 3, Figure 4d), respectively. In Figure 4, the MF-MHD model displays the maximum ionospheric ion and electron densities at the periapsis of orbit O2349 (on 14 December 2015), in good agreement with the MAVEN observation. Both the MF-MHD calculations and the MAVEN data reveal that O_2^+ is the dominant ion in the Martian ionosphere.

Compared with Case 1, the MF-MHD calculations based on the 3-D M-GITM thermosphere (Case 2) fit the observational data better, demonstrating the importance of adopting the 3-D thermosphere in a global plasma code. In Figure 4b, the calculated molecular ion (O_2^+ and CO_2^+) densities along the MAVEN trajectory are slightly higher than the Neutral Gas and Ion Mass Spectrometer data, while the O^+ ion density is slightly lower than that observed. Figure 4c, however, shows an opposite trend as presented in Figure 4b. In order to understand the deviation between simulations and observations, we plot both 1-D and 3-D thermospheric O and CO_2 densities along the MAVEN trajectory (Figure 5). As we expected, the 3-D thermosphere (Case 2) has a higher O and lower CO_2 abundance compared to the 1-D thermosphere (Case 1) along the MAVEN trajectory. This helps to explain the variation trend in the ion densities from Figures 4b to 4c. An inspection of

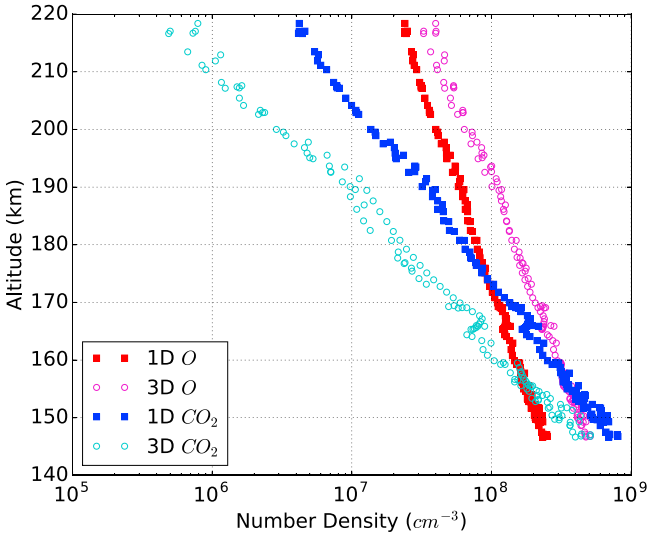

Figure 5. Comparisons between the 1-D and 3-D thermospheric density profiles along the Mars Atmosphere and Volatile EvolutioN trajectory. The plot includes both inbound and outbound data.

Figures 4c and 4d reveals that the 3-D hot oxygen does not have a significant effect on the ionospheric density distribution compared to the 1-D exosphere case.

Although we have presented the ionospheric ion densities along one MAVEN trajectory, it is also important to depict the global density distribution of the Martian ionosphere. Figure 6 illustrates the 2-D (latitude versus local time, at 200-km altitude) ionospheric maps from the MF-MHD model for Case 1 (left column) and Case 2 (right column). For both cases, the top panels show the density distribution of O^+, and the middle to bottom panels display the density distribution of O_2^+ and CO_2^+, respectively. The smooth transition of the ion density around terminator region is a result of the implementation of Chapman function from Smith and Smith (1972) in the MF-MHD model. Again, both columns show that O_2^+ is the dominant ion species in the Martian ionosphere. In order to better understand the different ion distributions shown in Figure 4, we also plotted the projection of the MAVEN trajectory in each panel.

In Figure 6 (left column), all the ions mirror a similar ionospheric pattern as a result of the 1-D spherically symmetric thermospheric input. The enhanced ion density in the southern hemisphere is mainly caused by the crustal magnetic fields given that the crustal anomalies are shifted to higher SZAs (i.e., the southern polar region in MSO) at aphelion. The same enhancement at the southernmost latitudes seen in the left column is not present in the right column because the 3-D asymmetric thermosphere (as shown in Figure 2) produces relatively high ion abundance at lower latitudes and northern hemisphere compared to the 1-D thermosphere case. In Figure 6 (right column), however, the ionospheric global distributions between molecular ions (O_2^+ and CO_2^+) and atomic ions (O^+) are distinct when adopting the 3-D thermosphere. On the other hand, O_2^+ and CO_2^+ share similar ionospheric patterns. It is well known that the Martian dayside ionosphere is triggered by the photoionization resulting from the solar extreme ultraviolet (EUV) radiation (Bougher et al., 2008). Subsequently, the photoionized CO_2^+ quickly reacts with neutral O to produce the major ionospheric species O_2^+; therefore, O_2^+ exhibits a similar ionospheric distribution as CO_2^+. The ionospheric density peaks of O_2^+ and CO_2^+ are also located at almost the identical altitude (e.g., see Figure 7). Although thermospheric O can be photoionized by photons (the main channel), ionized through charge exchange with other ion species, and impact ionized by electrons to produce O^+, the absence of the neutral oxygen atom (in the dayside thermosphere in the 3-D case) leads to a low abundance of O^+ in the dayside ionosphere (right column of Figure 6), consistent with the neutral density distribution shown in Figure 2. Compared with the previous work, O^+ in the present work can also be produced through photoionization of CO_2 as a secondary channel.

In order to understand the effect of the 3-D thermosphere on the ion escape, we calculate the ion escape rates and list them in Table 4. The calculations are conducted by integrals of the plasma density multiplied by the radial velocity component at the surface of a sphere far from the planet. Calculations (not presented here for the sake of brevity) show that ion escape rates do not change to any significant degree (<~5%) once the

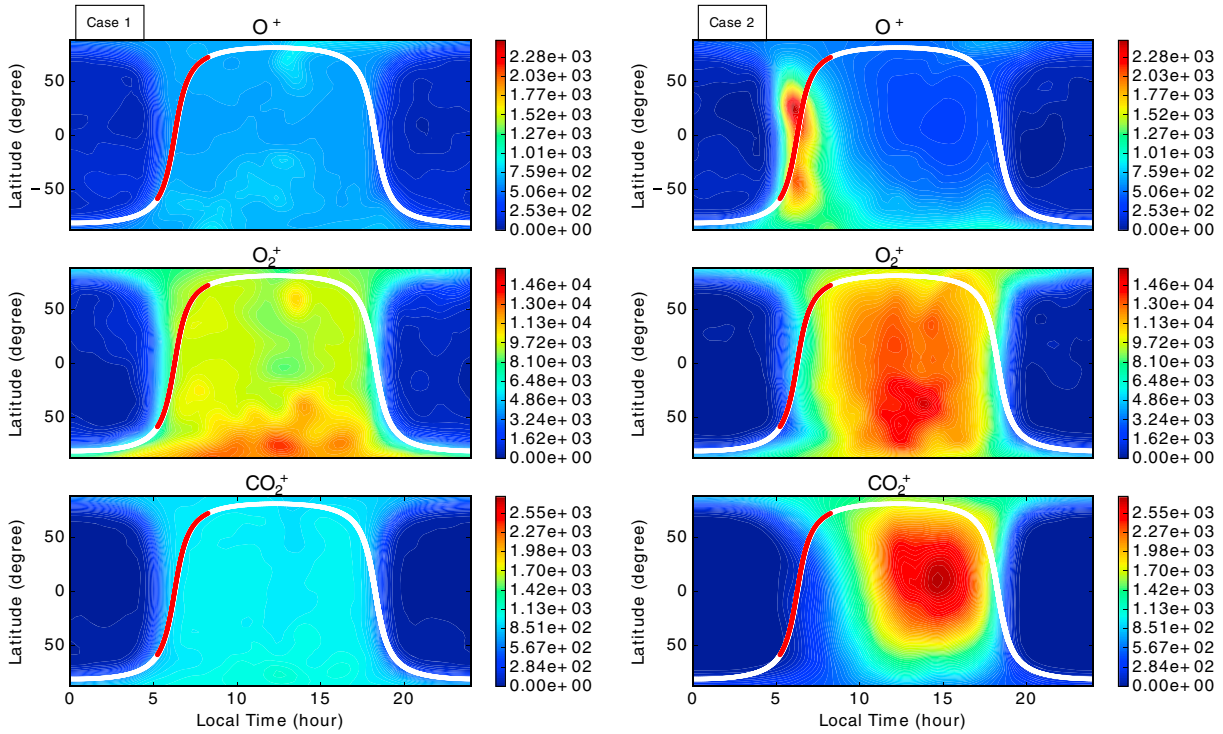

Figure 6. The ionospheric density maps for O^+, O_2^+, and CO_2^+ at 200-km altitude for Case 1 (left column) and Case 2 (right column). The thick white curve in each panel represents the projection of a selected Mars Atmosphere and Volatile EvolutioN trajectory (orbit O2349 on 14 December 2015). The red segment corresponds to the regions with altitudes lower than 1,000 km, including the periapsis. Note the use of different color bar range in different rows.

radius exceeds 5 R_M, the result presented in the remainder of this paper use the integral sphere with radius 6 R_M. Compared with Case 1 (with 1-D globally averaged thermosphere), the O^+ ion escape rate in Case 2 (with 3-D thermosphere) increases, while molecular ionospheric ion (O_2^+ and CO_2^+) escape rate decreases. These trends can be explained by the vertical ionospheric density profiles (at SZA = 0) shown in Figure 7. As seen from Figure 7, more O^+ at lower altitudes for Case 1 and more molecular ionospheric ions (O_2^+ and CO_2^+) at lower altitudes for Case 2, consistent with Figure 6. The relative abundance, however, shows a contrary trend at high altitudes (in the yellow shading region). Interestingly, the high-altitude ion abundance is consistent with the ion escape rates listed in Table 4 since only those ions above a certain altitude (i.e., ion exobase) are able to escape (e.g., Cravens et al., 2017). From test particle simulations, Fang et al. (2010b) also found that generally on the dayside, only less than 35% of ions are able to escape below 400-km altitude.

3.2. Effects of 3-D Exosphere on the Solar Wind-Mars Interaction

In order to investigate the effect of the 3-D exosphere (i.e., hot oxygen corona) on the interplay between the Martian upper atmosphere and the solar wind, we study three cases with a 1-D corona, a 3-D corona, and a case without a hot oxygen corona (Cases 2–4). This is similar to the study by Curry, Luhmann, Ma, Dong, et al. (2015), who conducted test particle simulations to study O^+ ion loss rates with and without the 1-D hot oxygen corona from Kim et al. (1998) by fixing the 1-D thermosphere from Ma et al. (2004).

3.2.1. Effects of 3-D Hot Oxygen Corona on O^+ Ion Escape

Figure 8 depicts the O^+ density in the $X - Z$ plane. One of the features of the MF-MHD model is that it can capture the asymmetric escape plume of the planetary pickup ions (Dong, Bougher, Ma, Toth, Nagy, et al., 2014; Najib et al., 2011; Rubin et al., 2014). Both Cases 2 and 3 present dayside pickup O^+ ion escaping from the extended hot oxygen corona region, while the high-altitude corona O^+ ions cannot be observed in Case 4 due to the absence of an atomic oxygen source. Compared with Case 2, more O^+ are present in the dayside exospheric region in Case 3, consistent with those hot oxygen density distributions shown in Figure 9. All three cases present a large number of O^+ ions escaping from the nightside plasma wake region as well. The color contours in Figure 8 can be used to explain why the O^+ ion escape rate of Case 2 is smallest among three cases and O^+ ion escape rates between Cases 3 and 4 are similar. The similar ion escape rate between Cases 3 and 4 implies that the thermospheric oxygen atoms make a significant contribution on the O^+ ion escape rate.

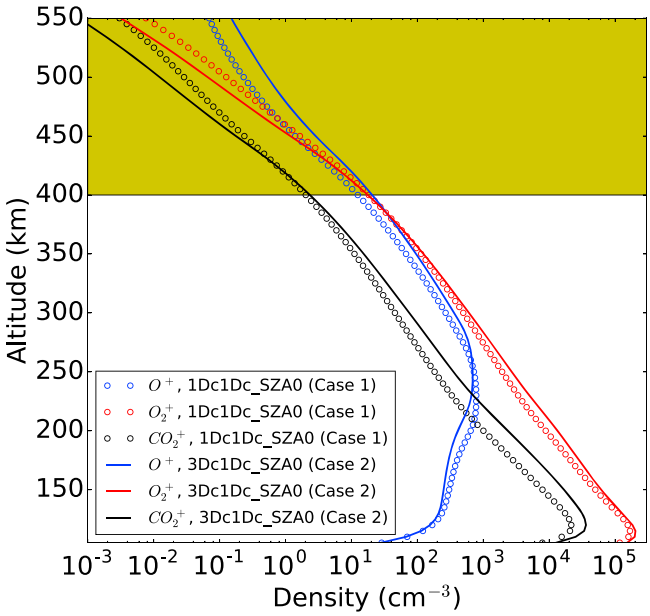

Figure 7. The vertical ionospheric density profiles for O^+, O_2^+, and CO_2^+ at SZA = 0 for Case 1 (circle markers) and Case 2 (solid curves). The yellow shading highlights a region that is more relevant to the ion escape. SZA = solar zenith angle.

3.2.2. Effects of 3-D Hot Oxygen Corona on Ion Escape: O^+ Versus (O_2^+ and CO_2^+)

In this section, we will focus on Cases 3 and 4 and aim to understand the effect of a 3-D hot oxygen on O^+ ion escape versus ionospheric molecular ion (O_2^+ and CO_2^+) losses. We summarize the calculated ion escape rates for Cases 3 and 4 in Table 4.

Compared with Case 3 that includes hot oxygen, Case 4 (without hot oxygen) has higher O_2^+ and CO_2^+ escape rates but maintains a similar value of O^+ escape rate. The variation in the molecular to atomic escaping ion ratio (i.e., the last column of Table 4) indicates that the hot oxygen component has a shielding effect that can protect the Martian ionosphere from the solar wind erosion, especially for O_2^+ and CO_2^+ that have a relatively high mass and thus are located at relatively low altitudes. It also reveals that the thermospheric oxygen is the dominant neutral source in determining the Martian O^+ ion escape for APHMOD under the nominal solar wind conditions.

Before proceeding further, recall that Dong, Bougher, et al. (2015) calculated the ion escape rates under different solar cycle and seasonal conditions. They found that O_2^+ is the dominant escaping ion at solar minimum, while O^+ is the dominant escaping species at solar maximum. Curry et al. (2013a) also showed the importance

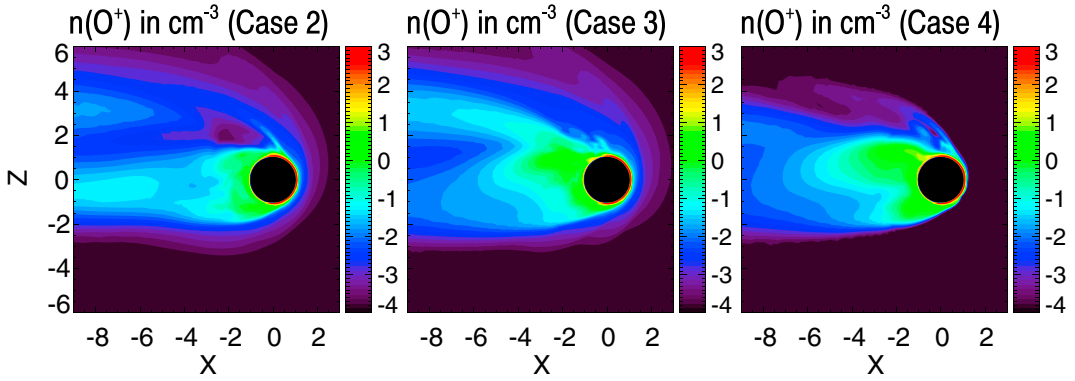

Figure 8. Comparison of O^+ density in the $X - Z$ plane for a 1-D corona, a 3-D corona, and a case without a hot oxygen corona. Left: case with the 1-D globally averaged hot oxygen corona (Case 2). Middle: case with the 3-D Mars Adaptive Mesh Particle Simulator hot oxygen corona (Case 3). Right: case without the hot oxygen corona (Case 4). Note the use of a logarithmic scale.

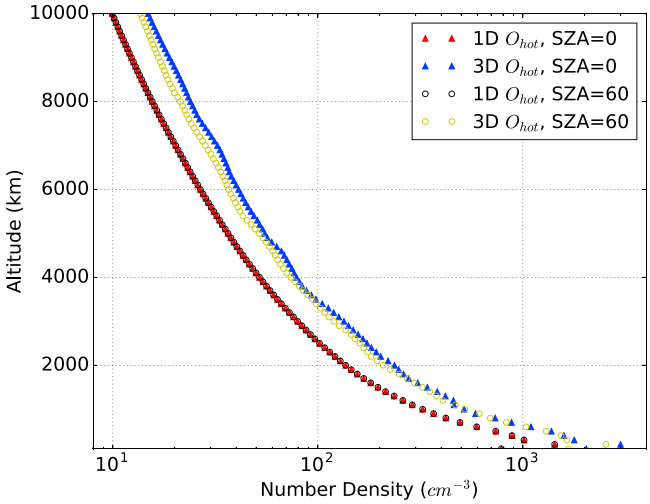

Figure 9. The comparison between 1-D and 3-D exospheric hot oxygen profiles at SZA = 0 and SZA = 60. SZA = solar zenith angle.

of O^+ ion escape using a test particle model at solar maximum. Therefore, we conduct a case study by choosing Case 10 (autumnal equinox solar maximum — AEQUMAX) in Dong, Bougher, et al. (2015) with and without 3-D hot oxygen corona; the O^+ ion escape rates are 4.57×10^{24} s^{-1} and 3.70×10^{24} s^{-1}, respectively. Compared with APHMOD, the hot oxygen becomes more important for O^+ ion escape at AEQUMAX. The thermospheric oxygen atom, however, is still the primary neutral source for O^+ ion escape for AEQUMAX under the nominal solar wind conditions.

The keys to understand the shielding effect of the hot oxygen corona are the ion pickup and mass loading processes. Given the momentum and energy conservation, the solar wind momentum and energy fluxes start to gradually decrease when approaching Mars due to the mass loading of high-altitude O^+ (ionized from hot oxygen corona). In the absence of a hot oxygen corona, the solar wind can directly interact with the Martian ionosphere and thermosphere.

Figure 10 demonstrates the solar wind proton number flux (left) and the electromagnetic energy density (right) at 1,000 km above the Martian surface for Cases 3 and 4. The electromagnetic energy density is defined as

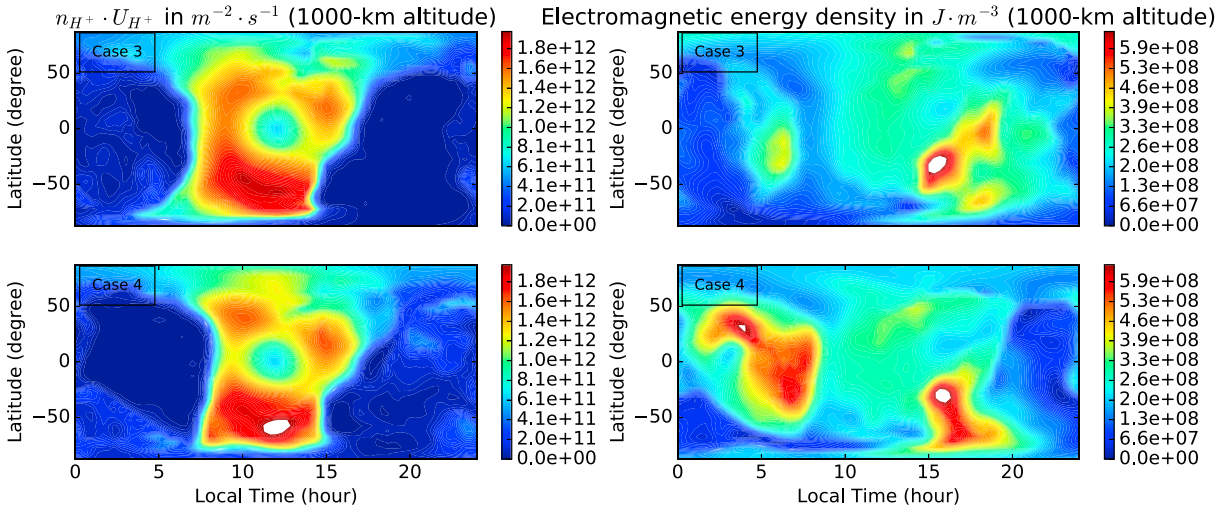

Figure 10. Comparison of the solar wind proton number flux, $n_{H^+}U_{H^+}$, between Cases 3 and 4 (left). Comparison of the electromagnetic energy density, $\mathcal{E}$, between Cases 3 and 4 (right). Both are depicted at 1,000-km altitude above the Martian surface. The white color highlights the regions beyond the high saturation of the color bar.

$$\mathcal{E} = \frac{\epsilon_0 E^2}{2} + \frac{B^2}{2\mu_0} \quad (1)$$

where ϵ_0 and μ_0 are the permittivity and permeability of free space, respectively. E denotes the electric field (see Equation (2) in Dong, Bougher, Ma, Toth, Nagy, et al., 2014), and B represents the magnetic field. In Figure 10 (left panel), the proton number flux in Case 4 is saturated at 1,000-km altitude (in white), while no saturation is observed in Case 3 using the same color bar range. Compared with Case 4, less electromagnetic energy density (right panel of Figure 10) is available at same altitude in Case 3, indicating that the ionosphere is more disturbed by the solar wind without a hot oxygen corona.

4. Conclusions

Recently, Dong, Lingam, et al. (2017) and Dong, Jin, et al. (2018) studied the atmospheric ion escape of exoplanets (such as Proxima b and the TRAPPIST-1 system by assuming Venus-like atmospheres) orbiting M dwarfs in the close-in habitable zone. Due to the strong EUV flux and extreme stellar wind parameters, they found that the O^+ ion is always the dominant escaping ion species (due to its relatively small mass and thus large-scale height) compared to O_2^+ and CO_2^+. In certain circumstances, the ionospheric molecular ion (O_2^+ and CO_2^+) escape rates of Venus-like exoplanets orbiting M dwarfs are similar to (and even smaller than) the cases in our solar system despite the much more intensive stellar radiation and stellar wind, as a result of the short star-planet distance, for example, 0.05 AU for Proxima b. The underlying reason is that the mass loading of relatively light O^+ ion slows down the stellar wind. At ancient times, the EUV flux and solar wind parameters were much stronger than that of the current epoch (partly resembling those of the M dwarf exoplanets discussed earlier), and Mars also has a much more extensive and intensive hot oxygen corona (Valeille et al., 2010), indicating that hot oxygen exosphere may provide an important source for O^+ ion escaping billions of years ago. Therefore, the hot oxygen corona may play a crucial role in the long-term evolution of the Martian atmosphere and its composition over its history (Dong, Bougher, Ma, Toth, Lee, et al., 2014; Dong, Lee, et al., 2018). Based on this study, we speculate that the early (e.g., 4 Gya) loss rate of the ionospheric molecular ions (O_2^+ and CO_2^+) may be even lower than the current value due to the strong shielding (i.e., mass loading) effect of high-altitude oxygen ions.

In summary, we studied the solar wind interaction with the Martian upper atmosphere using a one-way coupled framework of three comprehensive 3-D models, that is, the M-GITM thermosphere output and the Mars AMPS hot atomic oxygen corona are used as the input for the MF-MHD model. The effects of 1-D and 3-D cold thermosphere and hot oxygen corona on the ionospheric structure and ion escape rates are studied in detail by comparing four selected cases. While the total ion escape rates by adopting 1-D and 3-D neutral atmospheres are similar, the detailed ionospheric density distributions are distinguishable. Compared with the 1-D thermosphere, the MF-MHD calculations based on 3-D thermosphere are in better agreement with MAVEN observations. We also found that the hot oxygen corona plays an important role in protecting the Martian ionosphere and thermosphere from the solar wind erosion, that is, reducing the molecular ionospheric ion (O_2^+ and CO_2^+) escape rate. The shielding effect can be explained by the mass loading of the high-altitude hot oxygen ions. Moreover, the simulation results reveal that the cold atomic oxygen is the primary neutral source for O^+ ion escape during the relatively weak solar cycle 24.

Acknowledgments
The authors thank M. Lingam for the helpful discussions and comments. This research was supported by NASA grant NNH10CC04C through MAVEN project, and NASA grants 80NSSC18K0288, NNX14AH19G and NNX16AQ04G. Resources supporting this work were provided by the NASA High-End Computing (HEC) Program through the NASA Advanced Supercomputing (NAS) Division at Ames Research Center. We also would like to acknowledge high-performance computing support from Yellowstone (ark:/85065/d7wd3xhc) and Cheyenne (doi:10.5065/D6RX99HX) provided by NCAR's Computational and Information Systems Laboratory, sponsored by the National Science Foundation. The Space Weather Modeling Framework that contains the BATS-R-US code used in this study is publicly available from http://csem.engin.umich.edu/tools/swmf. The MAVEN data are publicly available through the Planetary Plasma Interactions Node of the Planetary Data System https://pds-ppi.igpp.ucla.edu/mission/MAVEN. The model results are publicly available at https://umich.box.com/s/tas6l27xzupb4dvkp2whz7k6wklnwes3.

References

Acuña, M. H., Connerney, J. E. P., Ness, N. F., Lin, R. P., Mitchell, D., & Carlson, C. W. (1999). Global distribution of crustal magnetization discovered by the Mars Global Surveyor MAG/ER experiment. *Science*, *284*, 790–793. https://doi.org/10.1126/science.279.5357.1676

Arkani-Hamed, J. (2001). A 50-degree spherical harmonic model of the magnetic field of Mars. *Journal of Geophysical Research*, *106*, 23,197–23,208.

Bird, G. A. (1994). *Molecular gas dynamics and the direct simulation of gas flows* (2nd ed.). Oxford: Clarendon Press.

Bougher, S. W., Blelly, P.-L., Combi, M. R., Fox, J. L., Mueller-Wodarg, I., Ridley, A., & Roble, R. G. (2008). Neutral upper atmosphere and ionosphere modeling. *Space Science Reviews*, *139*, 107–141. https://doi.org/10.1007/s11214-008-9401-9

Bougher, S. W., Cravens, T. E., Grebowsky, J., & Luhmann, J. (2015). The aeronomy of Mars: Characterization by MAVEN of the upper atmosphere reservoir that regulates volatile escape. *Space Science Reviews*, *195*, 423–456. https://doi.org/10.1007/s11214-014-0053-7

Bougher, S., Jakorsky, B., Halekas, J., Grebowsky, J., Luhmann, J., Mahaffy, P., et al. (2015). Early MAVEN Deep Dip campaign reveals thermosphere and ionosphere variability. *Science*, *350*, 0459. https://doi.org/10.1126/science.aad0459

Bougher, S. W., Pawlowski, D. J., Bell, J. M., Nelli, S., McDunn, T., Murphy, J. R., et al. (2015). Mars global ionosphere-thermosphere model (MGITM): Solar cycle, seasonal, and diurnal variations of the Mars upper atmosphere. *Journal of Geophysical Research: Planets*, *120*, 311–342. https://doi.org/10.1002/2014JE004715

Bougher, S. W., Roeten, K., Olsen, K., Mahaffy, P. R., Benna, M., Elrod, M., et al. (2017). The structure and variability of Mars dayside thermosphere from MAVEN NGIMS and IUVS measurements: Seasonal and solar activity trends in scale heights and temperatures. *Journal of Geophysical Research: Space Physics*, *122*, 1296–1313. https://doi.org/10.1002/2016JA023454

Brain, D. A., McFadden, J. P., Halekas, J. S., Connerney, J. E. P., Bougher, S. W., Curry, S., et al. (2015). The spatial distribution of planetary ion fluxes near Mars observed by MAVEN. *Geophysical Research Letters*, *42*, 9142–9148. https://doi.org/10.1002/2015GL065293

Brecht, S. H., Ledvina, S. A., & Bougher, S. W. (2016). Ionospheric loss from Mars as predicted by hybrid particle simulations. *Journal of Geophysical Research: Space Physics*, *121*, 10,190–10,208. https://doi.org/10.1002/2016JA022548

Cravens, T. E., Hamil, O., Houston, S., Bougher, S., Ma, Y., Brain, D., & Ledvina, S. (2017). Estimates of ionospheric transport and ion loss at Mars. *Journal of Geophysical Research: Space Physics*, *122*, 10,626–10,637. https://doi.org/10.1002/2017JA024582

Cravens, T. E., Kozyra, J. U., Nagy, A. F., Gombosi, T. I., & Kurtz, M. (1987). Electron impact ionization in the vicinity of comets. *Journal of Geophysical Research*, *92*, 7341–7353.

Curry, S. M., Liemohn, M., Fang, X., Brain, D., & Ma, Y. (2013b). Simulated kinetic effects of the corona and solar cycle on high altitude ion transport at Mars. *Journal of Geophysical Research: Space Physics*, *118*, 3700–3711. https://doi.org/10.1002/jgra.50358

Curry, S. M., Liemohn, M. W., Fang, X.-H., Ma, Y.-J., & Espley, J. (2013a). The influence of production mechanisms on pick-up ion loss at Mars. *Journal of Geophysical Research: Space Physics*, *118*, 554–569. https://doi.org/10.1029/2012JA017665

Curry, S. M., Liemohn, M. W., Fang, X.-H., Ma, Y.-J., Slavin, J., Espley, J., et al. (2014). Test particle comparison of heavy atomic and molecular ion distributions at Mars. *Journal of Geophysical Research: Space Physics*, *119*, 2328–2344. https://doi.org/10.1002/2013JA019221

Curry, S. M., Luhmann, J. G., Ma, Y. J., Dong, C. F., Brain, D., Leblanc, F., et al. (2015). Response of Mars O+ pick-up ions to the March 8th, 2015 ICME: Inferences from MAVEN data-based models. *Geophysical Research Letters*, *42*, 9095–9102. https://doi.org/10.1002/2015GL065304

Curry, S. M., Luhmann, J. G., Ma, Y., Liemohn, M. W., Dong, C., & Hara, T. (2015). Comparative pick-up ion distributions at Mars and Venus: Consequences for atmospheric deposition and escape. *Planetary and Space Science*, *115*, 35–47. https://doi.org/10.1016/j.pss.2015.03.026

Deng, Y., Richmond, A. D., Ridley, A. J., & Liu, H.-L. (2008). Assessment of the non-hydrostatic effect on the upper atmosphere using a general circulation model (GCM). *Geophysical Research Letters*, *35*, L01104. https://doi.org/10.1029/2007GL032182

DiBraccio, G. A., Luhmann, J. G., Curry, S. M., Espley, J. R., Xu, S., Mitchell, D. L., et al. (2018). The twisted configuration of the Martian magnetotail: MAVEN observations. *Geophysical Research Letters*, *45*, 4559–4568. https://doi.org/10.1029/2018GL077251

Dong, C., Bougher, S. W., Ma, Y., Toth, G., Lee, Y., Nagy, A. F., et al. (2014). Solar wind interaction with the Martian upper atmosphere at early Mars/extreme solar conditions. *AGU Fall Meeting Abstracts*, abstract P53C–4032.

Dong, C., Bougher, S. W., Ma, Y., Toth, G., Lee, Y., Nagy, A. F., et al. (2015). Solar wind interaction with the Martian upper atmosphere: Crustal field orientation, solar cycle and seasonal variations. *Journal of Geophysical Research: Space Physics*, *120*, 7857–7872. https://doi.org/10.1002/2015JA020990

Dong, C., Bougher, S. W., Ma, Y., Toth, G., Nagy, A. F., & Najib, D. (2014). Solar wind interaction with Mars upper atmosphere: Results from the one-way coupling between the multifluid MHD model and the MTGCM model. *Geophysical Research Letters*, *41*, 2708–2715. https://doi.org/10.1002/2014GL059515

Dong, Y., Fang, X., Brain, D. A., McFadden, J. P., Halekas, J. S., Connerney, J. E., et al. (2015). Strong plume fluxes at Mars observed by MAVEN: An important planetary ion escape channel. *Geophysical Research Letters*, *42*, 8942–8950. https://doi.org/10.1002/2015GL065346

Dong, C., Huang, Z., Lingam, M., Toth, G., Gombosi, T., & Bhattacharjee, A. (2017). The dehydration of water worlds via atmospheric losses. *The Astrophysical Journal Letters*, *847*, L4.

Dong, C., Jin, M., Lingam, M., Airapetian, V. S., Ma, Y. J., & van der Holst, B. (2018). Atmospheric escape from the TRAPPIST-1 planets and implications for habitability. *Proceedings of the National Academy of Sciences*, *115*, 260–265. https://doi.org/10.1073/pnas.1708010115

Dong, C., Lee, Y., Ma, Y., Lingam, M., Bougher, S., Luhmann, J., et al. (2018). Modeling martian atmospheric losses over time: Implications for exoplanetary climate evolution and habitability. *The Astrophysical Journal Letters*, *859*, L14. https://doi.org/10.3847/2041-8213/aac489

Dong, C., Lingam, M., Ma, Y. J., & Cohen, O. (2017). Is Proxima Centauri B habitable? A study of atmospheric loss. *The Astrophysical Journal Letters*, *837*, L26.

Dong, C., Ma, Y., Bougher, S. W., Toth, G., Nagy, A. F., Halekas, J. S., et al. (2015). Multifluid MHD study of the solar wind interaction with Mars' upper atmosphere during the 2015 March 8th ICME event. *Geophysical Research Letters*, *42*, 9103–9112. https://doi.org/10.1002/2015GL065944

Egan, H., Ma, Y., Dong, C., Modolo, R., Jarvinen, R., Bougher, S., et al. (2018). Comparison of global Martian plasma models in the context of MAVEN observations. *Journal of Geophysical Research: Space Physics*, *123*, 3714–3726. https://doi.org/10.1029/2017JA025068

Fang, X., Liemohn, M. W., Nagy, A. F., Luhmann, J. G., & Ma, Y. J. (2010a). On the effect of the Martian crustal magnetic field on atmospheric erosion. *Icarus*, *206*, 130–138. https://doi.org/10.1016/j.icarus.2009.01.012

Fang, X., Liemohn, M. W., Nagy, A. F., Luhmann, J. G., & Ma, Y. (2010b). Escape probability of Martian atmospheric ions: Controlling effects of the electromagnetic fields. *Journal of Geophysical Research*, *115*, A04308. https://doi.org/10.1029/2009JA014929

Fang, X., Liemohn, M. W., Nagy, A. F., Ma, Y., De Zeeuw, D. L., Kozyra, J. U., & Zurbuchen, T. H. (2008). Pickup oxygen ion velocity space and spatial distribution around Mars. *Journal of Geophysical Research*, *113*, A02210. https://doi.org/10.1029/2007JA012736

Fang, X., Ma, Y. J., Masunaga, K., Dong, Y. X., Brain, D., Halekas, J., et al. (2017). A quantitative study of the Mars crustal magnetic field control of plasma boundary locations and atmospheric loss: MHD prediction and comparison with MAVEN observations. *Journal of Geophysical Research: Space Physics*, *122*, 4117–4137. https://doi.org/10.1002/2016JA023509

Fox, J. L. (1993). On the escape of oxygen and hydrogen from Mars. *Geophysical Research Letters*, *20*, 1747–1750.

Glocer, A., Tóth, G., Ma, Y. J., Gombosi, T. I., Zhang, J. C., & Kistler, L. M. (2009). Multifluid Block-Adaptive-Tree Solar Wind Roe-Type Upwind Scheme: Magnetospheric composition and dynamics during geomagnetic storms—Initial results. *Journal of Geophysical Research*, *114*, A12203. https://doi.org/10.1029/2009JA014418

Halekas, J. S., Brain, D. A., Ruhunusiri, S., McFadden, J. P., Mitchell, D. L., Mazelle, C., et al. (2016). Plasma clouds and snowplows: Bulk plasma escape from Mars observed by MAVEN. *Geophysical Research Letters*, *43*, 1426–1434. https://doi.org/10.1002/2016GL067752

Harnett, E. M., & Winglee, R. M. (2006). Three-dimensional multifluid simulations of ionospheric loss at Mars from nominal solar wind conditions to magnetic cloud events. *Journal of Geophysical Research*, *111*, A09213. https://doi.org/10.1029/2006JA011724

Hassler, D. M., Zeitlin, C., Wimmer-Schweingruber, R. F., Ehresmann, B., Rafkin, S., Eigenbrode, J. L., et al. (2014). Mars' surface radiation environment measured with the Mars Science Laboratory's Curiosity rover. *Science*, *343*, 1244797.

Huang, Z. G., Toth, G., Gombosi, T. I., Jia, X. Z., Rubin, M., Fougere, N., et al. (2016). Four-fluid MHD simulations of the plasma and neutral gas environment of comet 67P/Churyumov-Gerasimenko near perihelion. *Journal of Geophysical Research: Space Physics*, *121*, 4247–4268. https://doi.org/10.1002/2015JA022333

Ip, W. H. (1988). On a hot oxygen corona of Mars. *Icarus*, *76*, 135.

Jakosky, B. M., Grebowsky, J, Luhmann, J. G., Connerney, J., Eparvier, F., Ergun, R., et al. (2015). MAVEN observations of the response of Mars to an interplanetary coronal mass ejection. *Science*, *350*, 0210. https://doi.org/10.1126/science.aad0210

Jakosky, B. M., Lin, R. P., Grebowsky, J, Luhmann, J. G., Mitchell, D. F., Beutelschies, G., et al. (2015). The Mars Atmosphere and Volatile Evolution (MAVEN) mission. *Space Science Reviews*, *195*, 3–48. https://doi.org/10.1007/s11214-015-0139-x

Johnson, R. E., & Luhmann, J. G. (1998). Sputter contribution to the atmospheric corona on Mars. *Journal of Geophysical Research*, *103*, 3649–3653.

Kharchenko, V., Dalgarno, A., Zygelman, B., & Yee, J. H. (2000). Energy transfer in collisions of oxygen atoms in the terrestrial atmosphere. *Journal of Geophysical Research*, *103*, 24,899–24,906.

Kim, J., Nagy, A. F., Fox, J. L., & Cravens, T. E. (1998). Solar cycle variability of hot oxygen atoms at Mars. *Journal of Geophysical Research*, *103*, 29,339.

Leblanc, F., Chaufray, J. Y., Modolo, R., Leclercq, L., Curry, S., Luhmann, J., et al. (2017). On the origins of Mars' exospheric nonthermal oxygen component as observed by MAVEN and modeled by HELIOSARES. *Journal of Geophysical Research: Planets*, *122*, 2401–2428. https://doi.org/10.1002/2017JE005336

Leblanc, F., Martinez, A., Chaufray, J. Y., Modolo, R., Hara, T., Luhmann, J., et al. (2018). On Mars' atmospheric sputtering after MAVEN first Martian year of measurements. *Geophysical Research Letters*, *45*, 4685–4691. https://doi.org/10.1002/2018GL077199

Lee, Y., Combi, M. R., Tenishev, V., Bougher, S. W., Deighan, J., Schneider, N. M., et al. (2015). A comparison of 3-D model predictions of Mars' oxygen corona with early MAVEN IUVS observations. *Geophysical Research Letters*, *42*, 9015–9022. https://doi.org/10.1002/2015GL065291

Lee, Y., Combi, M. R., Tenishev, V., Bougher, S. W., & Lillis, R. J. (2015). Hot oxygen corona at Mars and the photochemical escape of oxygen: Improved description of the thermosphere, ionosphere, and exosphere. *Journal of Geophysical Research: Planets*, *120*, 1880–1892. https://doi.org/10.1002/2015JE004890

Liemohn, M. W., Johnson, B. C., Franz, M., & Barabash, S. (2014). Mars Express observations of high altitude planetary ion beams and their relation to the "energetic plume" loss channel. *Journal of Geophysical Research: Space Physics*, *119*, 9702–9713. https://doi.org/10.1002/2014JA019994

Liemohn, M. W., Xu, S., Dong, C., Bougher, S. W., Johnson, B. C., Ilie, R., & De Zeeuw, D. L. (2017). Ionospheric control of the dawn-dusk asymmetry of the Mars magnetotail current sheet. *Journal of Geophysical Research: Space Physics*, *122*, 6397–6414. https://doi.org/10.1002/2016JA023707

Lillis, R. J., Brain, D. A., Bougher, S. W., Leblanc, F., Luhmann, J. G., Jakosky, B. M., et al. (2015). Characterizing atmospheric escape from Mars today and through time, with MAVEN. *Space Science Reviews*, *195*, 357–422. https://doi.org/10.1007/s11214-015-0165-8

Lingam, M., Dong, C. F., Fang, X. H., Jakosky, B. M., & Loeb, A. (2018). The propitious role of solar energetic particles in the origin of life. *The Astrophysical Journal*, *853*, 10.

Luhmann, J. G., Dong, C. F., Ma, Y. J., Curry, S. M., Mitchell, D., Espley, D., et al. (2015). Implications of MAVEN Mars near-wake measurements and models. *Geophysical Research Letter*, *42*, 9087–9094. https://doi.org/10.1002/2015GL066122

Luhmann, J. G., Dong, C. F., Ma, Y. J., Curry, S. M., Xu, S., Lee, C. O., et al. (2017). Martian magnetic storms. *Journal of Geophysical Research: Space Physics*, *122*, 6185–6209. https://doi.org/10.1002/2016JA023513

Luhmann, J. G., & Kozyra, J. U. (1991). Dayside pickup oxygen ion precipitation at Venus and Mars: Spatial distributions, energy deposition and consequences. *Journal of Geophysical Research*, *96*(A4), 5457–5467. https://doi.org/10.1029/90JA01753

Lundin, R., Barabash, S., Holmström, M., Nilsson, H., Futaana, Y., Ramstad, R., et al. (2013). Solar cycle effects on the ion escape from Mars. *Geophysical Research Letters*, *40*, 6028–6032. https://doi.org/10.1002/2013GL058154

Ma, Y. J., Fang, X., Russell, C. T., Nagy, A. F., Toth, G., Luhmann, J. G., et al. (2014). Effects of crustal field rotation on the solar wind plasma interaction with Mars. *Geophysical Research Letters*, *41*, 6563–6569. https://doi.org/10.1002/2014GL060785

Ma, Y. J., Nagy, A. F., Sokolov, I. V., & Hansen, K. C. (2004). Three-dimensional, multispecies, high spatial resolution MHD studies of the solar wind interaction with Mars. *Journal of Geophysical Research: Space Physics*, *109*, A07211. https://doi.org/10.1029/2003JA010367

Ma, Y. J., Russell, C. T., Fang, X., Dong, C. F., Nagy, A. F., Toth, G., et al. (2017). Variations of the Martian plasma environment during the ICME passage on 8 March 2015—A time-dependent MHD study. *Journal of Geophysical Research: Space Physics*, *41*, 1714–1730. https://doi.org/10.1002/2016JA023402

Mansfield, M., Kite, E. S., & Mischn, M. A. (2018). Effect of Mars atmospheric loss on snow melt potential in a 3.5 Gyr Mars climate evolution model. *Journal of Geophysical Research: Planets*, *123*, 794–806. https://doi.org/10.1002/2017JE005422

Modolo, R., Hess, S., Mancini, M., Leblanc, F., Chaufray, J.-Y., Brain, D., et al. (2016). Mars-solar wind interaction: LatHyS, an improved parallel 3-D multispecies hybrid model. *Journal of Geophysical Research: Space Physics*, *121*, 6378–6399. https://doi.org/10.1002/2015JA022324

Nagy, A. F., & Cravens, T. E. (1988). Hot oxygen atoms in the upper atmosphere of Venus and Mars. *Geophysical Research Letters*, *15*, 433–435. https://doi.org/10.1029/GL015i005p00433

Najib, D., Nagy, A. F., Tóth, G., & Ma, Y. J. (2011). Three-dimensional, multifluid, high spatial resolution MHD model studies of the solar wind interaction with Mars. *Journal of Geophysical Research*, *116*, A05204. https://doi.org/10.1029/2010JA016272

Powell, K. G., Roe, P. L., Linde, T. J., Gombosi, T. I., & De Zeeuw, D. L. (1999). A solution-adaptive upwind scheme for ideal magnetohydrodynamics. *Journal of Computational Physics*, *154*, 284–309.

Ramstad, R., Barabash, S., Futaana, Y., Nilsson, H., Wang, X.-D., & Holmström, M. (2015). The Martian atmospheric ion escape rate dependence on solar wind and solar EUV conditions I: Seven years of Mars Express observations. *Journal of Geophysical Research: Planets*, *120*, 1298–1309. https://doi.org/10.1002/2015JE004816

Ridley, A., Deng, Y., & Toth, G. (2006). The global ionosphere-thermosphere model. *Journal of Atmospheric and Solar - Terrestrial Physics*, *68*, 839.

Riousset, J. A., Paty, C. S., Lillis, C. S., Fillingim, M. O., England, S. L., Withers, P. G., & Hale, J. P. M. (2013). Three-dimensional multifluid modeling of atmospheric electrodynamics in Mars' dynamo region. *Journal of Geophysical Research: Space Physics*, *118*, 3647–3659. https://doi.org/10.1002/jgra.50328

Riousset, J. A., Paty, C. S., Lillis, R. J., Fillingim, R. J., England, S. L., Withers, P. G., & Hale, J. P. M. (2014). Electrodynamics of the Martian dynamo region near magnetic cusps and loops. *Geophysical Research Letters*, *41*, 1119–1125. https://doi.org/10.1002/2013GL059130

Rubin, M., Koenders, C., Altwegg, K., Combi, M. R., Glassmeier, K.-H., Gombosi, T. I., et al. (2014). Plasma environment of a weak comet—Predictions for Comet 67P/Churyumov–Gerasimenko from multifluid-MHD and Hybrid models. *Icarus*, *242*, 38–49.

Schunk, R. W., & Nagy, A. F. (2009). *Ionospheres* (2nd ed.). New York: Cambridge University Press. pp 102–109, chapter 8, pp 483.

Smith, F. L., & Smith, C. (1972). Numerical evaluation of Chapman's grazing incidence integral ch (X, χ). *Journal of Geophysical Research*, *77*, 3592–3597. https://doi.org/10.1029/JA077i019p03592

Tenishev, V., & Combi, M. (2008). A global kinetic model for cometary comae: The evolution of the coma of the Rosetta target comet Churyumov-Gerasimenko throughout the mission. *The Astrophysical Journal*, *685*, 659–677.

Tenishev, V., Rubin, M., Tucker, O. J., Combi, M. R., & Sarantos, M. (2013a). Kinetic modeling of sodium in the lunar exosphere. *Icarus*, *226*, 1538–1549. https://doi.org/10.1016/j.icarus.2013.08.021

Tóth, G., van der Holst, B., Sokolov, I. V., De Zeeuw, D., Gombosi, T. I., Fang, F., et al. (2012). Adaptive numerical algorithms in space weather modeling. *Journal of Computational Physics*, *231*, 870–903. https://doi.org/10.1016/j.jcp.2011.02.006

Valeille, A., Bougher, S. W., Tenishev, V., Combi, M. R., & Nagy, M. R. (2010). Water loss and evolution of the upper atmosphere and exosphere over Martian history. *Icarus*, *206*, 28–39. https://doi.org/10.1016/j.icarus.2009.04.036

Valeille, A., Tenishev, V., Bougher, S. W., Combi, M. R., & Nagy, A. F. (2009). Three-dimensional study of Mars upper thermosphere/ionosphere and hot oxygen corona: 1. General description and results at equinox for solar low conditions. *Journal of Geophysical Research*, *114*, E11005. https://doi.org/10.1029/2009JE003388

Wallis, M. K. (1978). Exospheric density and escape fluxes of atomic isotopes on Venus and Mars. *Planet and Space Science*, *26*, 949.

Withers, P., Vogt, M., Mayyasi, M., Mahaffy, P., Benna, M., Elrod, M., et al. (2015). Comparison of model predictions for the composition of the ionosphere of Mars to MAVEN NGIMS data. *Geophysical Research Letters*, *42*, 8966–8976. https://doi.org/10.1002/2015GL065205

Xu, S., Mitchell, D., Liemohn, M. W., Dong, C. F., Bougher, S., Fillingim, M., et al. (2016). Deep nightside photoelectron observations by MAVEN SWEA: Implications for Martian northern-hemispheric magnetic topology and nightside ionosphere source. *Geophysical Research Letters*, *43*, 8876–8884. https://doi.org/10.1002/2016GL070527